RSC Advances

ROYAL SOCIETY OF CHEMISTRY

PAPER

View Article Online
View Journal | View Issue

Cite this: *RSC Adv.*, 2022, **12**, 33419

Luminescence, energy transfer, colour modulation and up-conversion mechanisms of Yb^{3+}, Tm^{3+} and Ho^{3+} co-doped Y_6MoO_{12}†

Peng Guo,[a] Jiaxuan Wang,[a] Chuan Liao,[a] Haifeng Zhou,[b] Dapeng Huang,*[a] Guangjun Zhou, *[a] Xiaoqiang Yu [a] and Jifan Hu[a]

Received 7th September 2022
Accepted 15th November 2022

DOI: 10.1039/d2ra05642a

rsc.li/rsc-advances

A series of novel up-conversion luminescent Yb^{3+}/Ln^{3+} (Tm^{3+}, Ho^{3+}, Tm^{3+}/Ho^{3+})-doped Y_6MoO_{12} (YMO) nanocrystals were synthesized using the sol–gel method. The consistent spherical morphology of the nanocrystals with different doping ratios was found to be profiting from the homogenisation and rapid agglomeration of the composition in the gel state and calcining process. The X-ray diffraction (XRD) and field-emission scanning electron microscope images were employed to confirm perfect crystallinity and uniform morphology. Photoluminescence spectra and decay curves were used to characterize the optical properties of the synthesized samples. The YMO:Yb^{3+}/Ln^{3+} (Tm^{3+}, Ho^{3+}, Tm^{3+}/Ho^{3+}) nanocrystals were excited by near-infrared photons and emitted photons distributed in blue, green, and red bands with a wide colour gamut, and even white colour, by optimising the relative doping concentrations of the activator ions. The energy conversion mechanism in the up-conversion process was studied using power-dependent luminescence and is depicted in the energy level diagram. In addition, 70% of the luminescence intensity of YMO can be preserved after annealing at 700 °C, and the temperature sensing was tested in the range 298–498 K. These merits of multicolour emissions in the visible region and good stability endow the as-prepared nanocrystals with potential applications in the fields of optical data storage, encryption, sensing, and other multifunctional photonic technologies.

Introduction

Photon up-conversion (UC) is an anti-Stokes process in which the absorption of multiple low-energy photons leads to the emission of a photon with a higher energy than the excitation photon.[1–7] Rare-earth-doped up-conversion nanocrystals have garnered considerable attention because of their efficient energy transfer, good luminescence properties, and optical absorption ability,[8–11] which have significant applications in the fields of solid-state laser,[12,13] multicolour display,[14,15] optical data storage,[16,17] optical communication,[18,19] and optical sensing.[20,21] Ye and co-worker discovered a new non-contact optical material $Ba_3Y_4O_9$ for temperature measurement, and they achieved high sensitivity over a wide measuring temperature range.[22–24] Currently, complex application scenarios and multifunctional photonic technologies have put broad requirements for luminescent matrix materials with excellent chemical and thermal stability, accompanied by good up-conversion luminescence and colour tunability.[25–27]

Molybdate has emerged as an efficient matrix for luminescence.[28] The up-conversion luminescence (UCL) properties of various metal molybdates such as $BaMoO_4$ (ref. 29), $NiMoO_4$ (ref. 30), $Gd_2Mo_3O_9$ (ref. 31), $Gd_2(MoO_4)_3$ (ref. 32), and $CaMoO_4$ (ref. 33) are well documented in the literature. Y_6MoO_{12} (YMO) is an effective matrix of the molybdate family in luminescent materials.[34–36] The YMO crystal has a defect fluorite structure with a space group of $Fm\bar{3}m$, and the MoO_6 and YO_7 polyhedra have good chemical and thermal stability. Meanwhile, YMO has comparatively low phonon energies and high solubility of rare-earth (RE) ions owing to its large lattice tolerance. To date, Li *et al.*[28] investigated the photoluminescence (PL) properties of Eu^{3+}-doped YMO. Bieza *et al.*[37] investigated the optical properties of YMO doped with Yb^{3+} and successfully developed an optical ceramic. Several studies have demonstrated the excellent luminescence ability of the YMO matrix with good environmental tolerance, but UCL has not been realized owing to the absence of effective rare earth collocations and effective preparation methods.

It should be noted that lanthanides have a unique 4f electron configuration and an abundance of discrete energy levels. Among the rare-earth ions, Tm^{3+} and Ho^{3+} are usually used as efficient UC activators because of their high electronic

---

[a] *State Key Laboratory of Crystal Materials, Shandong University, Jinan, 250100, P. R. China. E-mail: gjzhou@sdu.edu.cn; dapenghuang@sdu.edu.cn*

[b] *School of Materials Science and Engineering, Qilu University of Technology (Shandong Academy of Sciences), Jinan, 250353, P. R. China*

† Electronic supplementary information (ESI) available. See DOI: **https://doi.org/10.1039/d2ra05642a**

structural symmetry, broadband absorption peaks, and excellent photon UC properties.[38,39] Moreover, two rare earth ions have been identified for outputting blue, green, and red visible photons under excitation by a 980 nm semiconductor laser, which can realize multiple colour adjustments and even white light to meet a wide range of optical storage, optical information encryption, anti-counterfeiting, and other intelligent photonics applications. However, the efficiency of photon up-conversion is low in the absence of sensitisers. Yb^{3+} ions can be used as sensitisers to enhance UC efficiency by considering their higher absorption cross-section near 980 nm and excellent energy transfer from Yb^{3+} to Tm^{3+} and Ho^{3+} ions.[40,41]

In this study, we report an efficient sol–gel method for the selective synthesis of high-purity disordered cubic fluorite-phase YMO with perfect crystallinity in doped YMO. Under optimal reaction conditions, the comparative multicolour UC photoluminescence properties and energy transfer mechanism of YMO:Yb^{3+}/Ln^{3+} (Tm^{3+}, Ho^{3+}, Tm^{3+}/Ho^{3+}) nanocrystals were investigated for different element ratios. The luminescence intensity and chromaticity coordinates could be adjusted by changing the Ln^{3+} concentration and species. In addition, the heat resistance of YMO was investigated, and its luminescence intensity can be preserved at 70% of its initial value after annealing at 700 °C. Moreover, we studied the potential temperature-sensing ability of YMO:Yb^{3+}:Tm^{3+}:Ho^{3+} phosphors. The merits of multicolour UCL and good stability enable the as-prepared Y_6MoO_{12} (YMO) nanocrystals to perform well for extensive applications in multifunctional photonic technologies.

Experimental

Materials and methodology

The starting materials, $Y(NO_3)_3$ (99.99%), $Yb(NO_3)_3$ (99.99%), $Tm(NO_3)_3$ (99.99%), $Ho(NO_3)_3$ (99.99%), $(NH_4)_6Mo_7O_{24}$ (99.98%), polyethylene glycol (PEG, 99%), and citric acid $C_6H_8O_7$ (>99.5%), were purchased from Macklin, and used without further purification. YMO:Yb^{3+}/Ln^{3+} (Tm^{3+}, Ho^{3+}, Tm^{3+}/Ho^{3+}) was synthesised using the sol–gel method and then calcined in a muffle furnace. Different concentrations of reagents were used according to experimental requirements, such as $Y_{99.7-y}MO{:}yYb^{3+}/0.3Tm^{3+}(y = 0\text{–}25)$, $Y_{80-t}MO{:}20Yb^{3+}/tTm^{3+}(t = 0.3\text{–}0.9)$, $Y_{80-h}MO{:}20Yb^{3+}/hHo^{3+}(h = 0.1\text{–}0.9)$ and $Y_{79.7-c}MO{:}20Yb^{3+}/0.3Tm^{3+}/cHo^{3+}(c = 0.25\text{–}1)$. Firstly, $Y(NO_3)_3$, $Yb(NO_3)_3$, $Tm(NO_3)_3$, $Ho(NO_3)_3$ and $Tm(NO_3)_3$/$Ho(NO_3)_3$ were doped at a set concentration and stirred to ensure uniform mixing. Citric acid was added and mixed thoroughly to form solution A. Then $(NH_4)_6Mo_7O_{24}$ (0.1428 mmol) and the corresponding proportion of citric acid were dissolved in deionised water to form solution B. This solution B was slowly added into solution A under stirring to form solution C. Subsequently, a certain amount of PEG was added, and the PH of the solution was adjusted to 2–3. The solution C was then stirred at 80 °C until a homogeneous sol–gel was formed and gradually converted to a highly concentrated brownish-yellow material. The gel was obtained by drying at 80 °C, for 12 h. The precursor was calcined in a muffle furnace at 700 °C for 4 h and cooled naturally to room temperature. The obtained samples were ground to a final powder for characterisation.

Result and discussion

The X-ray diffraction (XRD) patterns of Yb^{3+}/Tm^{3+}, Yb^{3+}/Ho^{3+}, and Yb^{3+}/Tm^{3+}/Ho^{3+}-doped YMO are shown in Fig. 1(a). All the diffraction peaks observed for the samples matched well with those of YMO (JCPD card no 30-1456). The absence of other miscellaneous peaks in Fig. 1(a) indicates that the doping of all ions did not cause any changes in the lattice and that the doped ions were well integrated into the lattice. Also, the high intensity of the peaks indicates that all the as-prepared samples have a high-purity phase and perfect crystallinity. According to the relevant literature,[37] the structure of Yb^{3+} is similar to that of Y^{3+}. Therefore, with the increase in the doping amount of Yb^{3+}, no new peak appeared in the XRD patterns of YMO, and the positions of the peaks remained the same. In addition, as shown in Fig. 1(a), doping with Tm^{3+} and Ho^{3+} ions similarly cause no lattice changes, probably because of the low doping concentration. The intrinsic and ion-doped YMO crystals have a disordered cubic fluorite structure with a space group of $Fm\bar{3}m$. The calculated lattice constant is $a = 5.29$ Å. The average size of the synthesised YMO samples calcined at 700 °C was reported to be 80.1 nm, calculated using the Debye–Scherrer formula ($D = k\lambda/\beta\cos\theta$)[42] and correlated well with the size determined from SEM analysis.

As depicted in a previous report,[37] the crystal structure of YMO was identical to that of Y_6WO_{12}, mainly because Mo^{6+} ions were completely replaced by W^{6+} ions. The prepared Re_6MoO_{12} material was successfully obtained by calcination at 700 °C for 4 h. Mo^{6+} ions occupy 3a (0, 0, 0) octahedral sites, and Y^{3+} ions occupy 18f (x, y, z) sites.[43] Mo^{6+} ions and the surrounding O^{2-} ions form MoO_6 octahedra, and other O^{2-} ions and Y^{3+} ions form a YO_7 polyhedron. As shown in Fig. 1(b), MoO_6 and YO_7 polyhedra are connected by sharing corners and edges. Because of the small difference between the ionic radii of the Yb^{3+} and Y^{3+} ions, the Yb^{3+} ions occupy the Y^{3+} site, and the lattice change caused by the doping of Yb^{3+} ions is negligible. Therefore, YMO doped with Yb^{3+} ions preserve the original crystal structure of YMO.

The size of the prepared nanocrystals was uniform, and the majority were 100 nm in size, which is smaller than the average size of reported YMO material.[37] As shown in Fig. 2, doping does not change the morphology or particle size, which is consistent with the XRD results. The consistent spherical particles and similar particle size resulted from the homogenisation and rapid agglomeration of the composition in the gel-state and calcining process. Meanwhile, polymer surfactants adjusted the nanocrystal growth kinetics by interacting with the crystal surfaces. Owing to the rapid oxidation reaction of the material during calcination, the gases escaped rapidly and the composition agglomerated rapidly, so that many pores and voids were found in the calcined samples.

Using a near-infrared laser ($\lambda_{ex} = 980$ nm) exciting the Yb^{3+}/Ln^{3+} (Ln = Tm^{3+}, Ho^{3+}, Tm^{3+}/Ho^{3+})-doped YMO at room temperature, we obtained a series of multi-colour tunable UCL

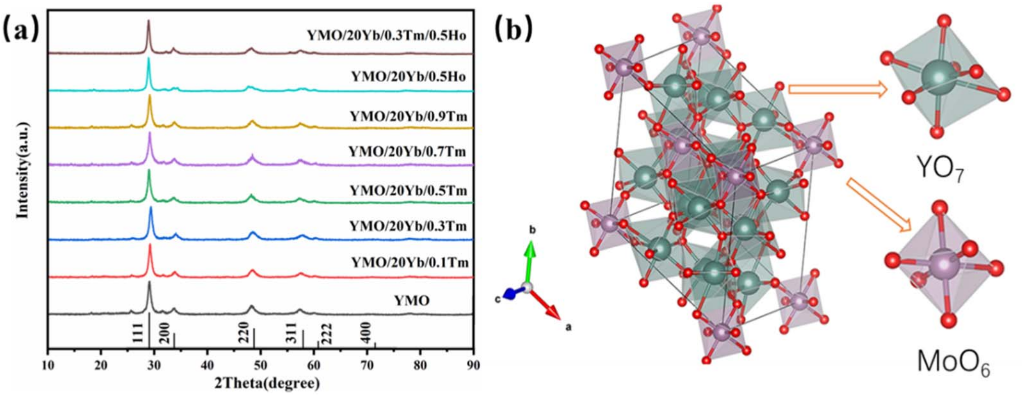

Fig. 1 (a) XRD patterns of the YMO:Yb^{3+}/Ln^{3+} (Tm^{3+}, Ho^{3+}, Tm^{3+}/Ho^{3+}) nanoparticles. (b) Visualisation of YMO cubic structure with MoO$_6$ and YO$_7$ polyhedra. Red atoms indicate the mixed rare earth molybdenum positions, green atoms indicate the mixed rare earth yttrium.

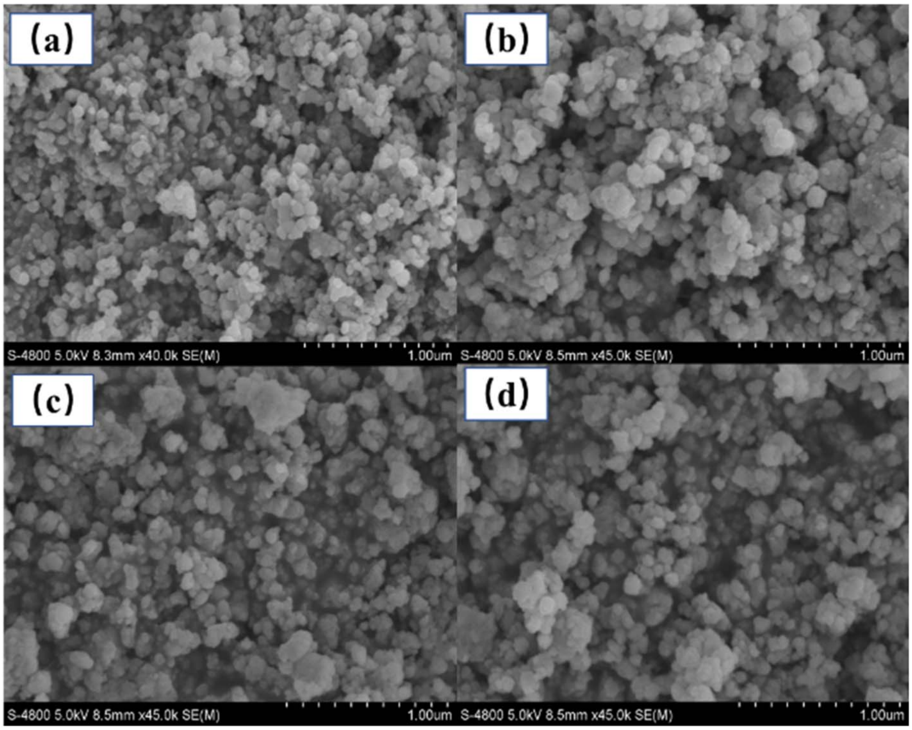

Fig. 2 FE-SEM images of the samples. (a) YMO, (b) YMO:20Yb^{3+}/0.3Tm^{3+}, (c) YMO:20Yb^{3+}/0.5Ho^{3+}, (d) YMO:20Yb^{3+}/0.3Tm^{3+}/0.75Ho^{3+}.

spectrum. As shown in Fig. 3(a), when the Tm^{3+} concentration is fixed at 0.3 mol%, with the change of Yb^{3+} doping amount, the luminescence phenomenon of the YMO made a significant change. In the blue and red ranges, there were two main emission peaks from the energy level transitions of $^1G_4 \rightarrow {}^3H_6$ and $^1G_4 \rightarrow {}^3F_4$ of Tm^{3+}. The inset in Fig. 3(a) clearly shows the change in luminescence intensity of the UCL with increasing doping concentration of Yb^{3+}, and at a doping concentration of 20 mol%, YMO has the best light intensity. When the Yb^{3+} doping concentration continued to increase, the fluorescence intensity showed a decreasing trend due to cross-relaxation losses. On this basis, YMO:20Yb^{3+}/tTm^{3+} nanocrystals with varying Tm^{3+} concentrations were studied comprehensively. As shown in Fig. 3(b) and the inset, the spectrum of Tm^{3+} ion doping sample has a strong blue light at 475.5 nm and a weak red light at 648 nm, corresponding to the transitions of ($^1G_4 \rightarrow {}^3H_6$) and ($^1G_4 \rightarrow {}^3F_4$). The luminescence intensities of the peaks in the blue and red bands were enhanced as the concentration of Tm^{3+} increased to 0.3 mol%. Subsequently, the increase in the Tm^{3+} concentration induced luminescence quenching.

Further, as shown in Fig. 3(c), (0.1–0.9 mol%) Ho^{3+}-doped YMO nanocrystals exhibit a weak green emission band ($^5F_4$, $^5S_2 \rightarrow {}^5I_8$) centred at 540 and 550 nm, a strong red emission band ($^5F_5 \rightarrow {}^5I_8$) centred at 660 nm, and a weak red emission band ($^5S_2 \rightarrow {}^5I_7$) centred at 757 nm. As shown in the inset of Fig. 3(c), when the Ho^{3+} ion concentration is low, such as 0.1 mol%,

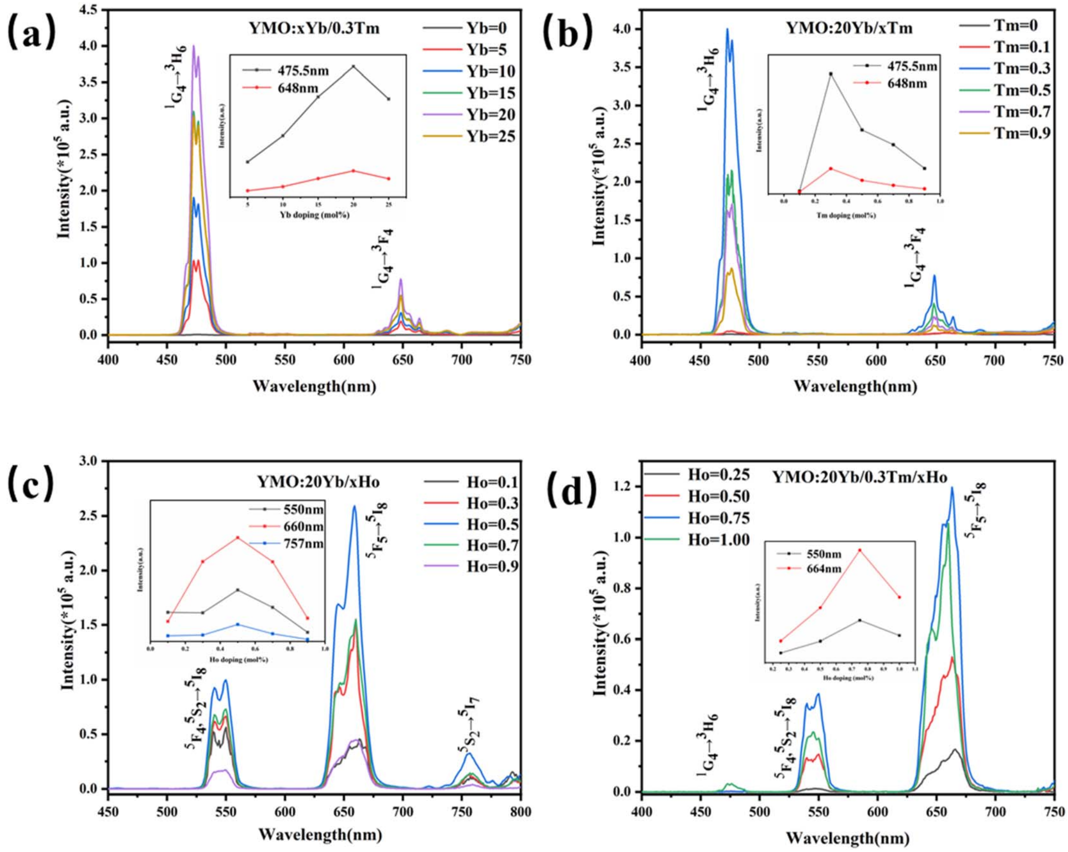

Fig. 3 The up-conversion emission (a): (0–25) Yb^{3+}/0.3Tm^{3+}, (b): 20Yb^{3+}/(0.1–0.9) Tm^{3+}, (c): 20Yb^{3+}/(0.1–0.9) Ho^{3+}, (d): 20Yb^{3+}/0.3Tm^{3+}/(0.25–1) Ho^{3+} and the percentage change in luminescence intensity with different concentrations of rare earth ion doping are embedded in the graphs under 980 nm laser excitation.

green and red emissions are relatively weak. With an increase in the Ho^{3+} concentration, the intensity of this luminescence gradually increased. A strong green luminescence was observed at a concentration of 0.50 mol%, and the intensity of the three peaks show a trend of gradually increased. According to the study of different doping concentrations, it was found that the highest intensity of green and red luminescence was observed at the concentration of 0.50 mol% Ho^{3+}, and the intensity of the three peaks was reduced due to the quenching of the concentration when the concentration of Ho^{3+} reached 1.00 mol%.

Fig. 3(d) shows the UCL spectra of Tm^{3+}/(0.1–0.9 mol%) Ho^{3+} ions doped in YMO nanocrystals. Blue (477 nm: $^1G_4 \rightarrow {}^3H_6$ of Tm^{3+} ions), green (547 nm and 550 nm: $^3F_4$, $^5S_2 \rightarrow {}^5I_8$ of Ho^{3+} ions), and red (664 nm: $^5F_5 \rightarrow {}^5I_8$ of Ho^{3+} ions) emissions were observed. As shown in the inset of Fig. 3(d), the red and green luminescence intensities are the highest when the Ho^{3+} ion concentration reached 0.75 mol%. However, when the Ho^{3+} ion concentration reached 1 mol%, blue light centred at 477 nm appeared. The emission of red light was stronger than that of blue and green lights. As shown in Fig. 3(d), the emission peaks are mainly generated from the Ho^{3+} ion, accompanied by energy transfer ($Yb^{3+} \rightarrow Tm^{3+} \rightarrow Ho^{3+}$).[44] However, the $^1G_4 \rightarrow {}^3H_6$ luminescence intensity of Tm^{3+} in Fig. 3(d) is substantially weaker, which may be due to the presence of cross-relaxation between Tm^{3+} and Ho^{3+}. This causes a remarkable decrease in the luminescence of Tm^{3+} ions. However, when the doping concentration of the Ho^{3+} ion is 1 mol%, owing to the quenching of the concentration, the energy level transition ($^1G_4 \rightarrow {}^3H_6$) of the Tm^{3+} ion can be boosted by the emission of blue light (477 nm). Lanthanide elements exhibit different UCL characteristics owing to their different electron configurations and energy level structures. Therefore, it is a good choice to control the doping concentration of Ho^{3+} in the YMO host and control its colour.

It is well known that UCL is an anti-Stokes luminescence process, in which two or more low-energy photons are successively absorbed, and then one high-energy photon is emitted in rapid succession. The relationship between the up-conversion luminescence intensity (denoted as I) and excitation power (denoted as P) is $I \propto P^n$, where I is the luminescence intensity, P is the infrared pump power, and n is a positive integer for the conversion of absorbed NIR photons to higher energies. Fig. 4(a–f) show the spectra of Yb^{3+}/Ln^{3+} (Tm^{3+}, Ho^{3+}, Tm^{3+}/Ho^{3+})-doped YMO at different powers.

As shown in Fig. 4(d), for the Yb^{3+}/Tm^{3+}-doped YMO up-conversion nanocrystals, the logarithmic plot of the luminescence intensities at 475.5 nm ($^1G_4 \rightarrow {}^3H_6$) and 648 nm ($^1G_4 \rightarrow {}^3F_4$) *versus* the input power present slope values of 1.576 and

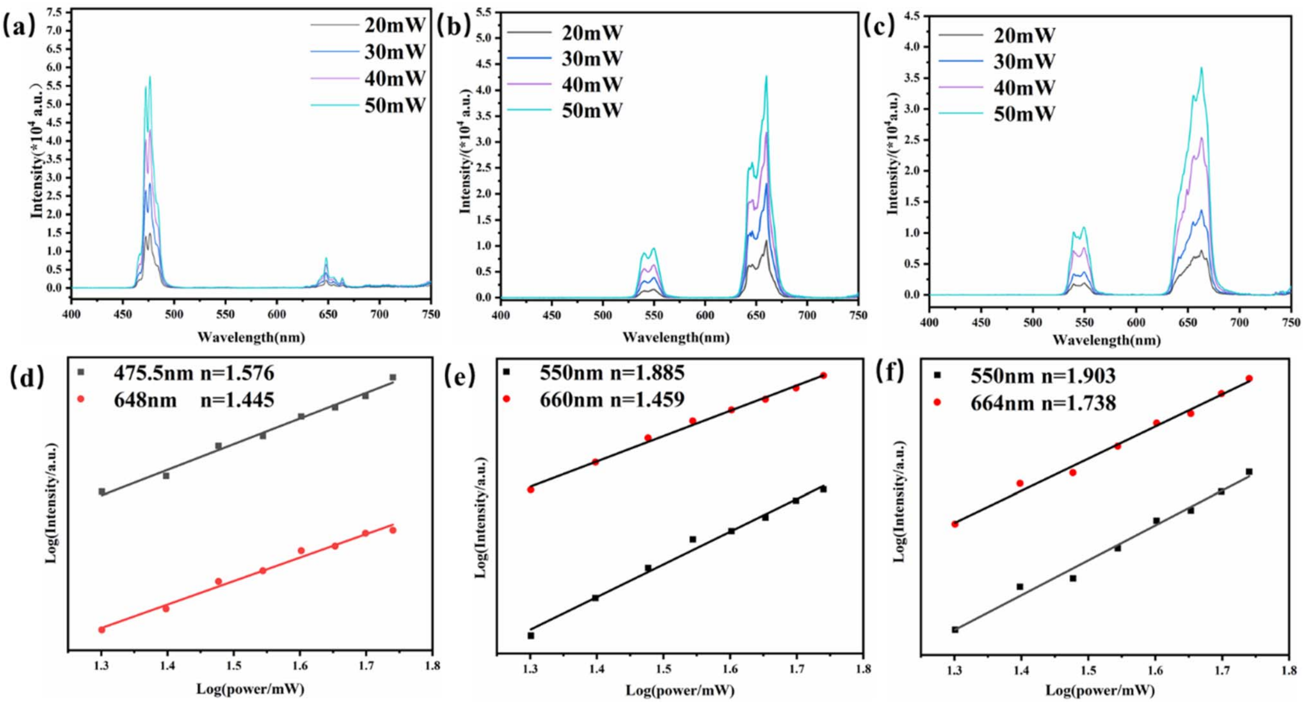

Fig. 4 Up-conversion spectra of YMO:Yb^{3+}/Ln^{3+} (Tm^{3+}, Ho^{3+}, Tm^{3+}/Ho^{3+}) under excitation of a 980 nm laser at the different power (a–c) and logarithmic plot of the luminescence intensities at different wavelength *versus* input power (d–f).

1.445. This result indicates that the mechanism responsible for the observed emission is UC photoluminescence dominated by two-photon absorption, in which the blue luminescence process is more dominant than that of red luminescence. Similarly, as shown in Fig. 4(e), for Yb^{3+}/Ho^{3+}-doped YMO, the power-dependent luminescence at 550 nm ($^5S_2 \rightarrow {}^5I_8$) and 660 nm ($^5F_5 \rightarrow {}^5I_8$) present slopes of 1.885 and 1.459, respectively, indicating that the luminescence processes are two-photon absorption processes. The values of n for YMO:$20Yb^{3+}$/$0.3Tm^{3+}$/$0.75Ho^{3+}$ with wavelengths of 550 nm ($^5S_2 \rightarrow {}^5I_8$) and 664 nm ($^5F_5 \rightarrow {}^5I_8$) are 1.903 and 1.738, respectively, which demonstrate the transition from Yb^{3+} to Tm^{3+} and Ho^{3+}, involving two NIR photons. When a photon is absorbed by the host, the energy loss and non-radiative relaxation result in the emission energy being less than the absorbed energy, therefore, the slopes are all less than 2.

To demonstrate the kinetic process of the UCL, we studied the decay curves of YMO:$20Yb^{3+}$,$0.3Tm^{3+}$ (monitored at 475.5 nm and 648 nm for $^1G_4 \rightarrow {}^3H_6$ and $^1G_4 \rightarrow {}^3F_4$), YMO:$20Yb^{3+}$,$0.5Ho^{3+}$ (monitored at 550 nm and 660 nm for $^5S_2 \rightarrow {}^5I_8$ and $^5F_5 \rightarrow {}^5I_8$), and YMO:$20Yb^{3+}$,$0.3Tm^{3+}$,$0.75Ho^{3+}$ (monitored at 550 nm and 664 nm for $^1G_4 \rightarrow {}^3H_6$ and $^1G_4 \rightarrow {}^3F_4$) under the excitation of a 980 nm laser. These samples can be fitted into a good double exponential formula as follows:

$$I(\tau) = I_1 \exp(-t/\tau_1) + I_2 \exp(-t/\tau_2),$$

where I indicates the luminescence intensity, I_1, τ_1 and I_2, τ_2 are the shorter and longer lifetime constants, respectively, and t is the time obtained τ_{ave} values, as shown in Fig. 5. Obviously, the fitting lifetimes τ for the $^5S_2 \rightarrow {}^5I_8$ and $^5F_5 \rightarrow {}^5I_8$ energy transfer of Ho^{3+} in the YMO:$20Yb^{3+}$,$0.5Ho^{3+}$ sample (29.44 μs and 87.51 μs, respectively) is bigger compared with those of the YMO:$20Yb^{3+}$,$0.3Tm^{3+}$,$0.50Ho^{3+}$ sample (12.97 μs and 18.71 μs, respectively), as shown in Fig. 5(b) and (c). This provides strong evidence of energy transfer (ET) from Tm^{3+} to Ho^{3+} by cross-relaxation process (CR) processes. With an increase in the Ho^{3+} ion concentration, the corresponding lifetime related to $^5S_2 \rightarrow {}^5I_8$ and $^5F_5 \rightarrow {}^5I_8$ are shortened (Fig. 5(d) and (e)), which is due to accelerated electrons relaxation rate with the increase of activator as some previously reported literature.[45,46] In addition, to gain a deeper understanding of the influence of Yb^{3+} ions on the cross-relaxation process (CR) of Ho^{3+} and Tm^{3+}, we carried out a comparison of the lifetimes of Tm^{3+} ions at different doping concentrations. As shown in Fig. 5(f) and (g), the possibility of an ET process between the two ions is further confirmed by measuring the luminescence decay curve. The detected wavelengths were 550, 664, and 796 nm at the $^5S_2$ and $^5F_5$ energy levels of Ho^{3+} and $^3H_4$ energy level of Tm^{3+}, respectively. With the increase in Tm^{3+} concentration, it is obvious that the decay lifetimes of the 550 and 664 nm emissions increase monotonously, and the lifetime of the 796 nm emissions decreases slightly. As stated in the article,[47] it could be attribute to the increased rate of the two CR processes between Tm^{3+} and Ho^{3+} ions at higher Tm^{3+} doping concentrations, accelerating the $^5S_2 \rightarrow {}^5I_8$ and $^5F_5 \rightarrow {}^5I_8$ photon radiative relaxation processes of the Ho^{3+} ions.

To compare the luminescence thermal stability of fluorides and oxides, $NaYF_4$ was prepared by referring our previous work,[25] and then YMO and $NaYF_4$ were annealed at 700 °C,

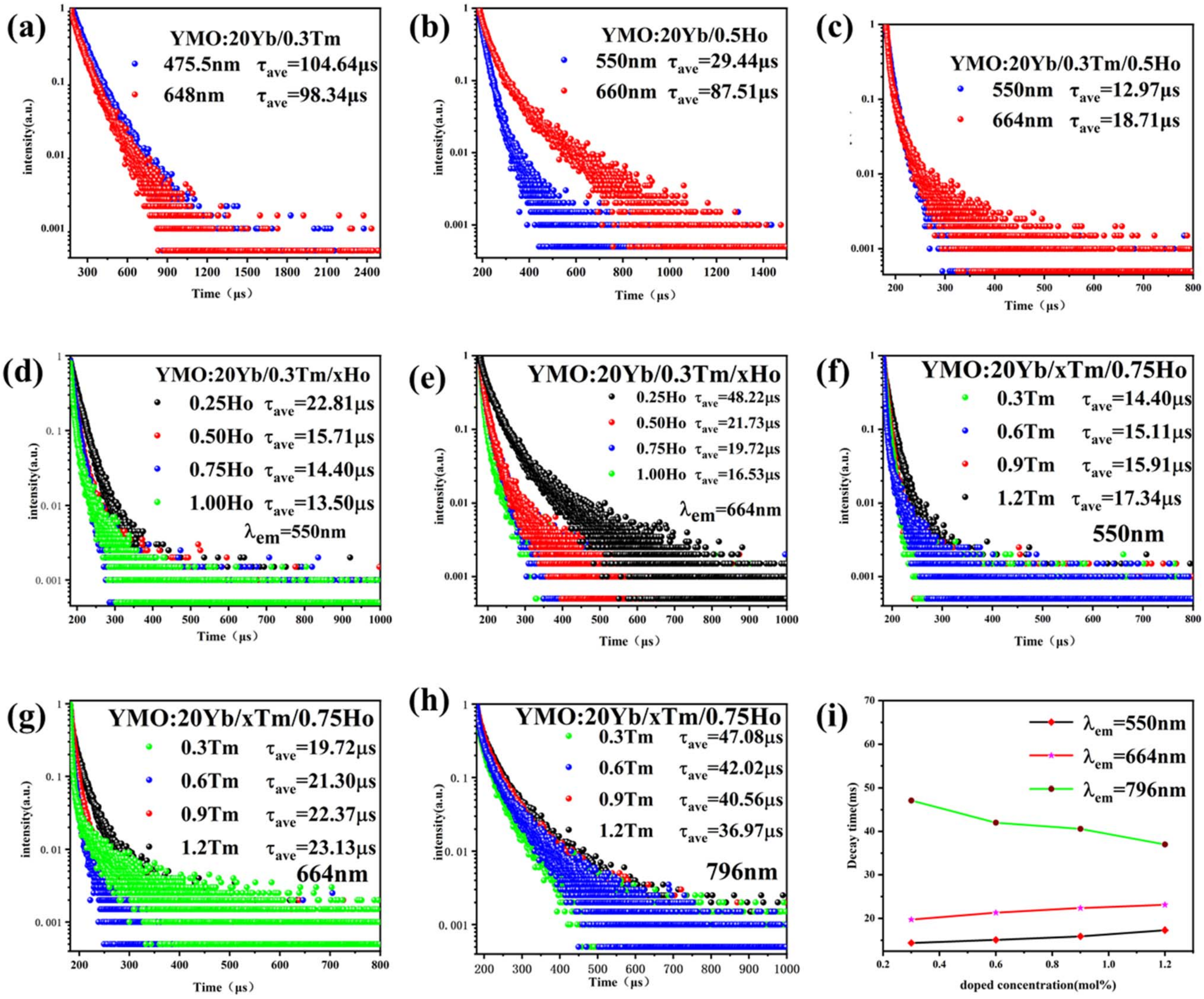

Fig. 5 Decay curves for samples under 980 nm excitation laser: (a) YMO/20Yb/0.3Tm, (b) YMO/20Yb/0.5Ho, (c) YMO/20Yb/0.3Tm/0.5Ho, (d) and (e) YMO/20Yb/0.3Tm/*x*Ho (*x* = 0.25, 0.50, 0.75, 1.00%) at 550 nm, 664 nm, (f)–(h) YMO/20Yb/*x*Tm/0.75Ho (*x* = 0.3, 0.6, 0.9, 1.2%) at 550 nm, 664 nm, and 796 nm, (i) the calculated decay times of corresponding emission energy levels.

respectively. The resulting luminescence spectra are shown in Fig. 6. It can be seen from the emission spectrum that the luminescence intensity of YMO sample and $NaYF_4$ sample decreased to 70% and 6.4% of the original after annealing at 700 °C, respectively. The luminescence decay of $NaYF_4$ sample was more obvious due to the phase transition (β → α) at

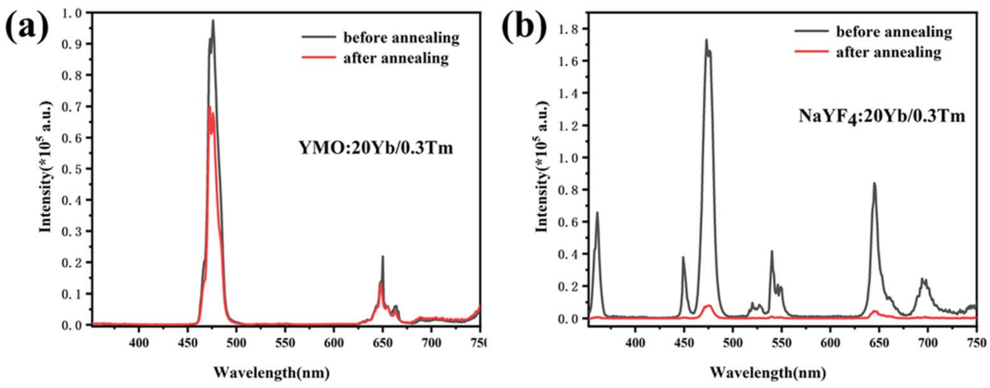

Fig. 6 Luminescence spectra before and after annealing: (a) YMO:Yb^{3+},Tm^{3+}, (b) $NaYF_4$:Yb^{3+},Tm^{3+}.

annealing process, which were verified by the XRD and TEM (Fig. S1 and S2†). The results clearly show that the luminescence thermal stability of YMO is much better than that of $NaYF_4$ as heated up to 700 °C.

To enable a better understanding of the UC luminescence mechanism of YMO:Yb^{3+}/Tm^{3+}/Ho^{3+} materials at different temperatures, the samples are collected at temperatures from 298 K to 498 K, as shown in Fig. 7(a). It describes the normalised temperature-dependent 550 nm emission spectra of the sample to deeply comprehend the responses of the green emissions to temperature. It is clearly observed that the emission intensities of triple-doped YMO are gradually quenched with increasing temperature. The FIR values between the $^5S_2 \rightarrow {}^5I_8$ and $^5F_5 \rightarrow {}^5I_8$ transitions at various temperatures are calculated according to the recorded UC emission spectra, as shown in Fig. 7(b). With a reasonable approximation, the relation between FIR and absolute temperature can be expressed by the following expression:[22,23]

$$\mathrm{FIR} = \frac{I_\mathrm{U}}{I_\mathrm{L}} = A\exp\left(\frac{-\Delta E}{kT}\right),$$

where I_U and I_L are the integrated emission intensities of the upper and lower thermally coupled levels, respectively, A is a constant, ΔE is the energy gap, and k is the Boltzmann constant. The values of A and $\Delta E/k$ were obtained as 4.69 and 787.5 by fitting the data. Fig. 7(c) shows the value of ln(FIR) as a function of absolute temperature. The above expression can also be rewritten as:

$$\ln(\mathrm{FIR}) = B + \frac{-\Delta E}{kT},$$

where B is a constant and ΔE refers to the energy gap. The data points can be fitted with a straight line, which confirms the suitability of the phosphor for temperature-sensing applications. The slope and intercept of the fitted line were approximately −756.3 and 1.469, respectively. To demonstrate the suitability of the studied samples for temperature detection, the sensor sensitivity at different temperatures (*i.e.*, absolute sensor sensitivity (S_A) and relative sensor sensitivity (S_R)) should be discussed. According to this report, the values of S_A and S_R as a function of temperature can be obtained from the following expression:[22,23]

$$S_\mathrm{A} = \frac{\mathrm{dFIR}}{\mathrm{d}T} = \mathrm{FIR} \times \frac{\Delta E}{kT^2}$$

$$S_\mathrm{R} = \frac{1}{\mathrm{FIR}}\frac{\mathrm{dFIR}}{kT^2} \times 100\% = \frac{\Delta E}{kT^2} \times 100\%$$

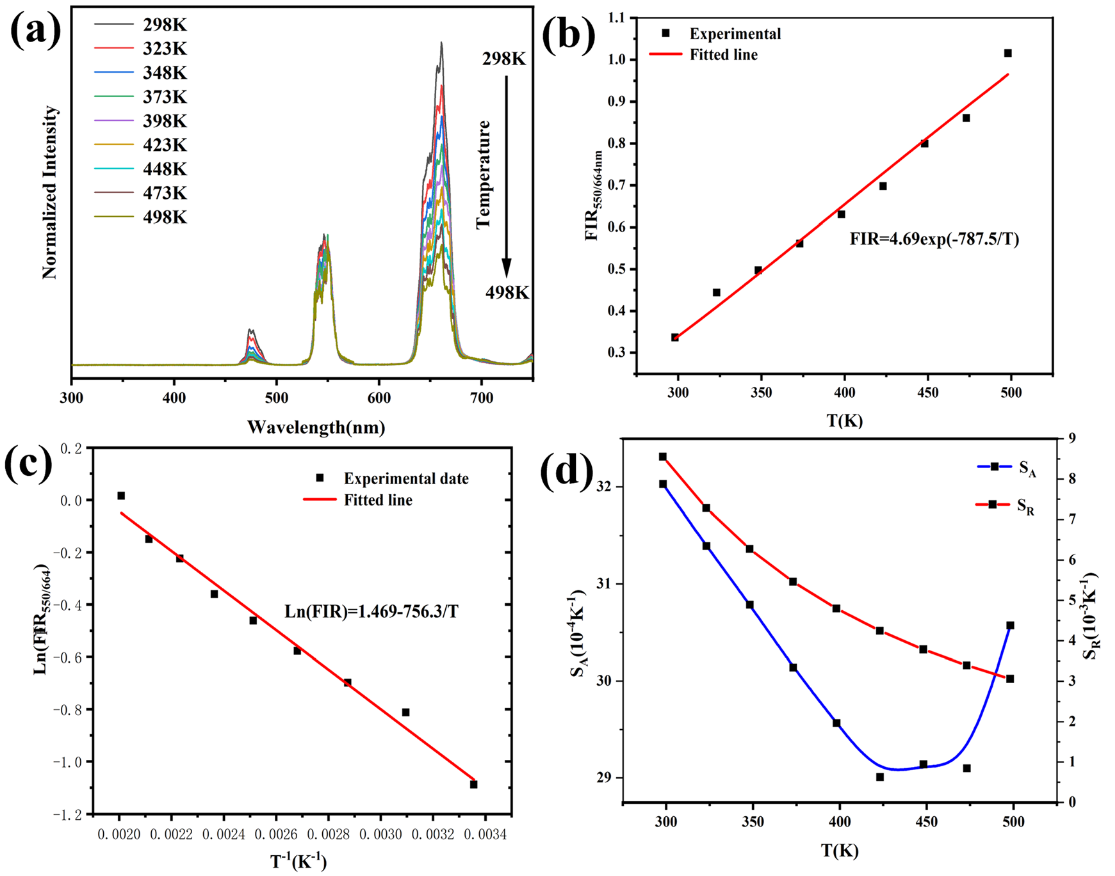

Fig. 7 (a) Normalized 550 nm emission spectra of the YMO:20Yb^{3+}:0.3Tm^{3+}:1Ho^{3+} microparticles in the temperature range 298–498 K. (b) FIR value as function of temperature and (c) plot of ln(FIR) *versus* T^{-1} for the YMO:20Yb^{3+}:0.3Tm^{3+}:1Ho^{3+} microparticles. (d) S_R and S_A values of the YMO:20Yb^{3+}:0.3Tm^{3+}:1Ho^{3+} microparticles as a function of temperature.

Fig. 7(d) depicts the correlation between S_A and S_R values, as derived from equations FIR and ln(FIR) equations. The absolute sensitivity S_A gradually increased with increasing temperature, with a maximum value of 0.0032 K^{-1}. The maximum S_R value is 0.85% K^{-1}. The optical temperature sensing performance of this work and other RE doped materials are shown in Table S1.† The absolute sensitivity (S_A) of YMO-based material shows a certain advantage among some oxides.[48–51] In addition, the temperature range of YMO is wider than that of molybdate $Gd_2Mo_3O_9$ [52] and the relative sensitivity (S_R) of YMO is higher than Y_2WO_6.[49]

The CIE coordinates of the YMO:Yb^{3+}/Ln^{3+} ($t$$Tm^{3+}$, $h$$Ho^{3+}$, Tm^{3+}/$c$$Ho^{3+}$) samples under 980 nm laser excitation are shown in Fig. 8 and Table 1. As the doping type of Ln^{3+} changed, there were distinct differences in the CIE coordinates. Because the energy level jump of the same doping type in the luminescence process is fixed, the change in the doping concentration of the sensitiser has little effect on the luminescence colour, and the CIE coordinates show aggregation by the same doping type with different concentrations. For Tm^{3+} ion doping, the luminescence peak is mainly concentrated in the blue region because the energy level transition from $^1G_4 \rightarrow {}^3H_6$ is greater than that from $^1G_4 \rightarrow {}^3F_4$, leading to the sample being mainly blue. In addition, the material achieves white up-conversion luminescence at a Tm^{3+} ion doping concentration of 0.1 mol%. Upon doping with Ho^{3+} alone, the luminescence colour is mainly yellow in CIE. For the double doping of Tm^{3+} and Ho^{3+} ions, it can be found that the luminescence region is mainly in the red-light region because of the leading emission peaks at 655 nm:$^1G_4 \rightarrow {}^3F_4$ of Tm^{3+} ions and 664 nm:$^5F_5 \rightarrow {}^5I_8$ of Ho^{3+} ions. Thus, by adjusting the concentrations of Tm^{3+} and Ho^{3+} ions, multi-colour tunable UCL over a wide gamut in the YMO matrix can be achieved.

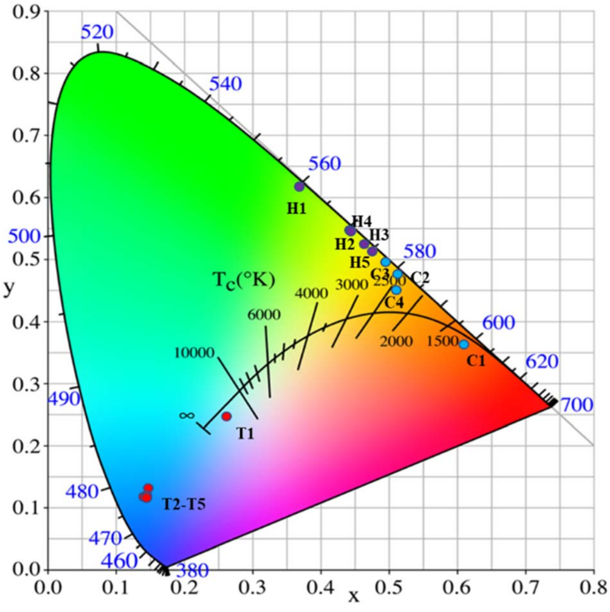

Fig. 8 CIE chromaticity diagram for YMO:20Yb,*t*Tm (T1–T5), YMO:20Yb,*h*Ho (H1–H5), and YMO:20Yb,0.3Tm,*c*Ho (C1–C4).

Table 1 Variations of CIE chromaticity coordinates for YMO:20Yb,*t*Tm (T1–T5), YMO:20Yb,*h*Ho (H1–H5), and YMO:20Yb,0.3Tm,*c*Ho (C1–C4)

No. of points	YMO:20Yb:*t*Tm	CIE (x, y)
T1	$t = 0.1$	(0.2609, 0.2435)
T2	$t = 0.3$	(0.1451, 0.1183)
T3	$t = 0.5$	(0.1431, 0.1159)
T4	$t = 0.7$	(0.1412, 0.1176)
T5	$t = 0.9$	(0.1480, 0.1334)
No. of points	YMO:20Yb:*h*Ho	CIE (x, y)
H1	$h = 0.1$	(0.3711, 0.6191)
H2	$h = 0.3$	(0.4453, 0.5464)
H3	$h = 0.5$	(0.4639, 0.5260)
H4	$h = 0.7$	(0.4773, 05448)
H5	$h = 0.9$	(0.4772, 0.5153)
No. of points	YMO:20Yb:0.3Tm:*c*Ho	CIE (x, y)
C1	$c = 0.25$	(0.6107, 0.3641)
C2	$c = 0.5$	(0.5119, 0.4773)
C3	$c = 0.75$	(0.4961, 0.4968)
C4	$c = 1$	(0.5124, 0.4514)

The main mechanisms of the UCL include ground state/excited state absorption (GSA/ESA), energy transfer (ET) up-conversion, and photon avalanche (PA). To clarify the filling mechanism of the UCL, the energy level diagrams of YMO:Yb^{3+},Tm^{3+}, YMO:Yb^{3+},Ho^{3+} are shown in Fig. 9. Because the slope does not change in Fig. 4, in principle, it does not involve the PA mechanism. Thus, the UCL process can be described as follows: first, the sensitiser Yb^{3+} ions absorb the near-infrared light at a wavelength of 980 nm, which leads to photon pumping from the ground state ($^2F_{7/2}$) to the excited state ($^2F_{5/2}$). Then the energy is transferred to Tm^{3+} (ET1: $^3H_5$, ET2: $^3F_{2,3}$, ET3: $^1G_4$) and Ho^{3+} (ET4: $^5I_6$, ET5: $^5F_4$, $^5S_2$), leading to the electron jumping from the ground state to the corresponding excited state, simultaneously with Yb^{3+} absorbing the energy again and transferring. The energy is then further transferred to the activator, and as the activator absorbs further energy, their electron energy levels further leap to higher energy levels. As the electrons continue to reach the corresponding highest excited state energy levels, the electrons continue to leap back to the ground state by radiation, eventually leading to UCL. For the Tm^{3+} ions, the energy absorbed by the Yb^{3+} ion was transferred to the ground state energy level of Tm^{3+}, leading to an energy level leap of $^3H_6 \rightarrow {}^3H_5$ (ET1), followed by a radiation-free relaxation of the $^3H_5$ energy level to energy level $^3F_4$. Subsequently, the Yb^{3+} ions transfer the energy absorbed again to energy level $^3F_4$ (ET2), causing it to leap to energy level $^3F_{2,3}$. The electrons at this energy level further relax to energy level $^3H_4$, which then leaps to $^1G_4$ by absorbing the energy absorbed by the Yb^{3+} ions (ET3) energy level and then radiating $^1G_4 \rightarrow {}^3H_6$ (475.5 nm) and $^1G_4 \rightarrow {}^3F_4$ (648 nm), respectively. For YMO:Yb^{3+},Ho^{3+}, the energy of the Yb^{3+} ions is transferred to the Ho^{3+} ions, which excites its electrons from the ground state $^5I_8$ to excited state $^5I_6$ (ET4), while the Yb^{3+} ions again transfer the

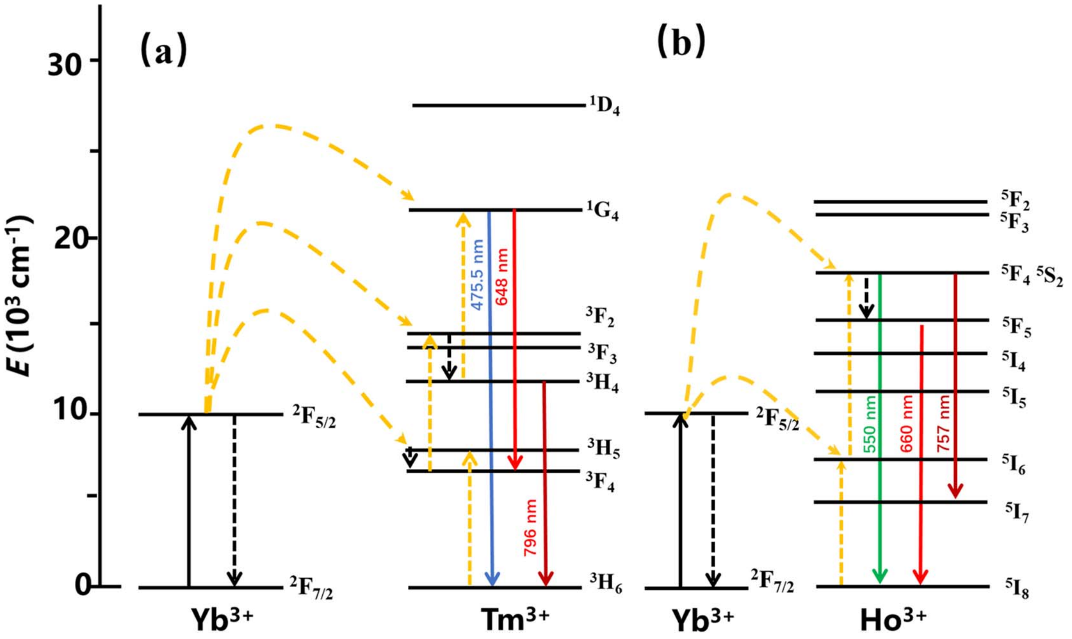

Fig. 9 The energy level diagram for the Tm^{3+} ion is (a) and the energy level diagram for the Ho^{3+} ion is (b).

absorbed energy to Ho^{3+} ions (ET5), which causes its energy level to jump $^5I_6 \rightarrow {}^5F_4$, $^5S_2$, and then some electrons in the excited state energy level leap back to the ground state, such as $^5F_4$, $^5S_2 \rightarrow {}^5I_8$ (550 nm), and $^5S_2 \rightarrow {}^5I_7$ (757 nm), and the remaining electrons relax to energy level $^5F_5$ and then further relax to the new $^5I_8$ emitting an intense red light (660 nm).

The energy transfer process of Yb^{3+} → Tm^{3+} → Ho^{3+} can be decomposed into the ET process of Yb^{3+} → Tm^{3+} and the CR process of Tm^{3+} → Ho^{3+}. After Yb^{3+} transfers energy to the Tm^{3+} energy level, a portion of the energy level relaxes, leading to $^1G_4 \rightarrow {}^3H_6$ and $^5S_2 \rightarrow {}^5I_7$, and excess energy is transferred to the Ho^{3+} ion energy level *via* the CR process, leading to $^5S_2 \rightarrow {}^5I_8$ and $^5F_5 \rightarrow {}^5I_8$. Combining the change in $^1G_4 \rightarrow {}^3H_6$ luminescence intensity in the conversion of YMO:20Yb,*t*Tm, and YMO:20Yb,0.3Tm,*c*Ho in Fig. 3 and the related arguments in the lifetime of Fig. 5, it can be concluded that energy transfer process takes in Yb^{3+} → Tm^{3+} → Ho^{3+}.

Conclusions

YMO materials were successfully prepared using a simple sol–gel method and subsequent combustion, and UCL results were obtained. Furthermore, the excellent heat resistance of YMO as an UC luminescent host was demonstrated. The results of XRD and SEM showed that the samples are disordered cubic fluorite structure with homogeneous spherical grains. The samples were irradiated with a 980 nm laser to obtain luminescence of different colours. The power-dependent UCL spectra indicated that YMO:Yb^{3+}/Ln^{3+} (Tm^{3+}, Ho^{3+}, Tm^{3+}/Ho^{3+}) was the dominant two-photon absorption process. In addition, the corresponding mechanisms, including the energy level transfer and phonon relaxation processes, were discussed in detail. Also, YMO:Yb^{3+}/Ln^{3+} (Tm^{3+}, Ho^{3+}, and Tm^{3+}/Ho^{3+}) has been verified with potential applications in optical temperature sensing.

Conflicts of interest

There are no conflicts to declare.

Acknowledgements

This work was supported by Shandong Province Science and Technology Program (2022TSGC1016); Foundation of Shandong Industrial Technology Research Institute (Z1250020007, Z1250020008); the National Natural Science Foundation of China (52102007, 51472150) and China Postdoctoral Science Foundation (2020M682175).

References

1 H. Huang, H. Zhou, J. Zhou, T. Wang, D. Huang, Y. Wu, L. Sun, G. Zhou, J. Zhan and J. Hu, *RSC Adv.*, 2017, **7**, 16777–16786.
2 M. Haase and H. Schafer, *Angew. Chem., Int. Ed. Engl.*, 2011, **50**, 5808–5829.
3 X. Xie, Z. Li, Y. Zhang, S. Guo, A. I. Pendharkar, M. Lu, L. Huang, W. Huang and G. Han, *Small*, 2017, **13**, 1602843.
4 Y. Kaoru, M. Fujii, S. Sowa, K. Imakita and K. Aoki, *J. Phys. Chem. C*, 2015, **119**, 1175–1179.
5 S. Xu, X. Xie, B. Zhao, L. Nie, Y. Pan, H. Su, L. Huang and W. Huang, *J. Rare Earth*, 2017, **35**, 28–33.
6 S. Liu, Z. An and B. Zhou, *Chem. Eng. J.*, 2023, **452**, 139649.
7 H. Huang, T. Wang, H. Zhou, D. Huang, Y. Wu, G. Zhou, J. Hu and J. Zhan, *J. Alloys Compd.*, 2017, **702**, 209–215.
8 Y. Yao, S. Zhang, H. Zhang, J. Ding, T. Jia, J. Qiu and Z. Sun, *Sci. Rep.*, 2014, **4**, 7295.
9 B. Zhang, J. Meng, X. Mi, C. Zhang, Z. Zhang and H. Zheng, *RSC Adv.*, 2018, **8**, 37618–37622.

10 L. T. K. Giang, K. Trejgis, L. Marciniak, N. Vu and L. Q. Minh, *Sci. Rep.*, 2020, **10**, 14672.

11 R. K. Sharma, M. Ghora, Y. N. Chouryal, T. Ganguly, D. Acharjee, D. J. Mondal, S. Konar, S. Nigam and P. Ghosh, *ACS Omega*, 2022, **7**, 16906–16916.

12 K. V. Krishnaiah, E. S. de Lima Filho, Y. Ledemi, G. Nemova, Y. Messaddeq and R. Kashyap, *Sci. Rep.*, 2016, **6**, 21905.

13 Y. L. Wang, N. Mohammadi Estakhri, A. Johnson, H. Y. Li, L. X. Xu, Z. Zhang, A. Alu, Q. Q. Wang and C. K. Shih, *Sci. Rep.*, 2015, **5**, 10196.

14 M. Kermorgant, J. Ben Salem, J. Santelli, D. Calise, A. C. Oster, O. Lairez, C. Coudret, M. Verelst, C. Gales, J. M. Senard, F. Beaudry, A. Pavy-Le Traon, C. Roux, R. Mauricot and D. N. Arvanitis, *PLoS One*, 2019, **14**, 0225729.

15 G. Chen, T. Y. Ohulchanskyy, R. Kumar, H. Agren and P. N. Prasad, *ACS Nano*, 2010, **4**, 3163–3168.

16 Y. Han, H. Li, Y. Wang, Y. Pan, L. Huang, F. Song and W. Huang, *Sci. Rep.*, 2017, **7**, 1320.

17 S. Lamon, Y. Wu, Q. Zhang, X. Liu and M. Gu, *Sci. Adv.*, 2021, **7**, 2209.

18 F. Huang, X. Liu, Y. Ma, S. Kang, L. Hu and D. Chen, *Sci. Rep.*, 2015, **5**, 8233.

19 X. Chen, X. Zhu, Y. Hu, W. Yuan, X. Qiu, T. Jiang, C. Xia, L. Xiong, F. Li and Y. Gao, *Theranostics*, 2020, **10**, 3281–3292.

20 K. Green, K. Huang, H. Pan, G. Han and S. F. Lim, *Front. Chem.*, 2018, **6**, 416.

21 Y. Bai, Y. Li, R. Wang and Y. Li, *ChemistrySelect*, 2021, **6**, 10263–10273.

22 S. Liu, J. Cui, J. Jia, J. Fu, W. You, Q. Zeng, Y. Yang and X. Ye, *J. Phys. Chem. C*, 2018, **122**, 16289–16303.

23 S. Liu, H. Ming, J. Cui, S. Liu, X. Ye, Y. Yang, H. Nie and R. Wang, *Ceram. Int.*, 2019, **45**, 1–10.

24 S. Liu, L. Yan, J. Huang, Q. Zhang and B. Zhou, *Chem. Soc. Rev.*, 2022, **51**, 1729.

25 T. Wang, H. Feng, Z. Chao, G. Jun, J. Juan, D. Peng, L. Sun, P. Guo, Y. Sun and J. Hu, *J. Phys. Chem. C*, 2018, **122**, 10113–10124.

26 B. Wu, L. Zhao, Y. Wang, H. Dong and H. Yu, *RSC Adv.*, 2019, **9**, 42228–42235.

27 Y. Shang, S. Hao, C. Yang and G. Chen, *Nanomaterials*, 2015, **5**, 1782–1809.

28 H. Li, X. Pu, S. Yao, X. Wang, H. M. Noh and J. H. Jeong, *J. Nanosci. Nanotechnol.*, 2016, **16**, 3636–3640.

29 S. K. Ray, Y. K. Kshetri, T. Yamaguchi, T.-H. Kim and S. W. Lee, *J. Solid State Chem.*, 2019, **272**, 87–95.

30 S. K. Ray, B. Joshi, S. Ramani, S. Park and J. Hur, *J. Alloys Compd.*, 2022, **892**, 162101.

31 J. Sun, B. Xue, G. Sun and D. Cui, *J. Rare Earth*, 2013, **31**, 741–744.

32 A. Kumari, A. K. Soni and V. K. Rai, *Infrared Phys. Technol.*, 2017, **81**, 313–319.

33 J. H. Chung, J. H. Ryu, S. Y. Lee, S. H. Kang and K. B. Shim, *Ceram. Int.*, 2013, **39**, 1951–1956.

34 G. George, V. S. Vishnu and M. L. P. Reddy, *Dyes Pigm.*, 2011, **88**, 109–115.

35 X. Zhao, Y. Zhang, Y. Huang, H. Gong and J. Zhao, *Dyes Pigm.*, 2015, **116**, 119–123.

36 M. Sobota, P. Sobota, M. Bieza, M. Guzik, E. Tomaszewicz, Y. Guyot and G. Boulon, *Opt. Mater.*, 2019, **90**, 300–314.

37 M. Bieza, M. Guzik, E. Tomaszewicz, Y. Guyot and G. Boulon, *Opt. Mater.*, 2017, **63**, 3–12.

38 Z. Ding, Y. He, H. Rao, L. Zhang, W. Nguyen, J. Wang, Y. Wu, C. Han, C. Xing, C. Yan, W. Chen and Y. Liu, *Nanomaterials*, 2022, **12**, 1787.

39 M. Secu, C. Secu and C. Bartha, *Materials*, 2021, **14**, 6871.

40 X. Zhao, Z. Wu, Z. Yang, X. Yang, Y. Zhang, M. Yuan, K. Han, C. Song, Z. Jiang, H. Wang, S. Li and X. Xu, *Nanomaterials*, 2020, **10**, 1475.

41 S. Shukla, P. C. Pandey and R. J. Narayan, *Polymers*, 2021, **13**, 2694.

42 S. B. Somvanshi, P. B. Kharat, T. Saraf, S. B. Somwanshi, S. B. Shejul and K. M. Jadhav, *Mater. Res. Innovations*, 2021, **25**, 169–174.

43 N. Diot, P. Benard-Rocherulle and R. Marchand, *Powder Diffr.*, 2000, **15**, 220.

44 H. Zhang, D. Sun, J. Luo, F. Peng, Z. Fang, X. Zhao, C. Quan, M. Cheng, Q. Zhang and S. Yin, *J. Lumin.*, 2018, **194**, 636–640.

45 X. Ye, Y. Luo, S. L. D. Hou and W. You, *J. Alloys Compd.*, 2017, **701**, 806–815.

46 S. Liu, X. Ye, S. Liu, M. Chen, H. Niu, D. Hou and W. You, *J. Am. Ceram. Soc.*, 2017, **100**, 3530–3539.

47 S. Liu, S. Liu, H. Ming, F. Du, J. Peng, W. You and X. Ye, *J. Mater. Sci.*, 2018, **53**, 14469–14484.

48 H. Liu, X. Zheng, P. Wang, H. Wang and Y. Zhang, *J. Opt. Soc. Am. B*, 2022, **39**, 2625.

49 J. Zhang, B. Ji, G. Cheng and Z. Hua, *Inorg. Chem.*, 2018, **57**, 5038–5047.

50 E. Maurice, G. Monnom, B. Dussardier, A. Saissy, D. B. Ostrowsky and G. W. Baxter, *Appl. Opt.*, 1995, **34**, 34.

51 P. V. dos Santos, M. T. de Araujo and A. S. Gouveia-Neto, *Appl. Phys. Lett.*, 1998, **28**, 578.

52 S. Sinha, M. K. Mahata and K. Kumar, *RSC Adv.*, 2016, **6**, 89642–89654.